Surface-Facet-Dependent Phonon Deformation Potential in Individual Strained Topological Insulator Bi₂Se₃ Nanoribbons
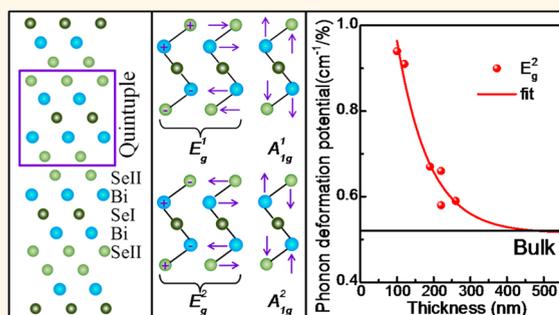
Yuan Yan,*,†,# Xu Zhou,‡,§,# Han Jin,‡,# Cai-Zhen Li,‡ Xiaoxing Ke,⊥ Gustaaf Van Tendeloo,⊥ Kaihui Liu,‡,‖,§ Dapeng Yu,‡,‖,§ Martin Dressel,† and Zhi-Min Liao*,‡,‖

†Physikalisches Institut, Universität Stuttgart, 70550 Stuttgart, Germany, ‡State Key Laboratory for Mesoscopic Physics, Department of Physics, Peking University, 100871 Beijing, China, §Academy for Advanced Interdisciplinary Studies, Peking University, 100871 Beijing, China, ⊥EMAT (Electron Microscopy for Materials Science), University of Antwerp, Groenenborgerlaan 171, B-2020 Antwerp, Belgium, and ‖Collaborative Innovation Center of Quantum Matter, Beijing, China. #These authors contributed equally to this work.

ABSTRACT Strain is an important method to tune the properties of topological insulators. For example, compressive strain can induce superconductivity in Bi₂Se₃ bulk material. Topological insulator nanostructures are the superior candidates to utilize the unique surface states due to the large surface to volume ratio. Therefore, it is highly desirable to monitor the local strain effects in individual topological insulator nanostructures. Here, we report the systematical micro-Raman spectra of single strained Bi₂Se₃ nanoribbons with different thicknesses and different surface facets, where four optical modes are resolved in both Stokes and anti-Stokes Raman spectral

lines. A striking anisotropy of the strain dependence is observed in the phonon frequency of strained Bi₂Se₃ nanoribbons grown along the ⟨11$\bar{2}$0⟩ direction. The frequencies of the in-plane E_g^2 and out-of-plane A_{1g}^1 modes exhibit a nearly linear blue-shift against bending strain when the nanoribbon is bent along the ⟨11$\bar{2}$0⟩ direction with the curved {0001} surface. In this case, the phonon deformation potential of the E_g^2 phonon for 100 nm-thick Bi₂Se₃ nanoribbon is up to 0.94 cm^{-1}/%, which is twice of that in Bi₂Se₃ bulk material (0.52 cm^{-1}/%). Our results may be valuable for the strain modulation of individual topological insulator nanostructures.

KEYWORDS: topological insulator · Bi₂Se₃ nanoribbon · Raman spectroscopy · strain · phonon confinement effect

Topological insulators (TIs) are a new class of quantum matter that possess a trivial insulating bulk phase and robust nontrivial metallic surface states.[1−5] They are considered as promising candidates for novel electronic applications beyond silicon in current electronic world, attracting enormous efforts from both theoretical and experimental research. Among the TIs family, Bi₂Se₃ has been proven to be an ideal candidate for studying topological surface states due to its simple energy band structure and relatively large bulk band gap of ∼0.3 eV.[6] The pressure induced phase transition from normal to superconducting phases in topological insulator Bi₂Se₃,[7,8] Bi₂Te₃,[9,10] and Sb₂Te₃[11] bulk materials have been reported; however, ultrahigh pressure

is required and a full understanding of the interplay between superconductivity and topological surface states is still elusive.[12,13] Compared to bulk materials, nanostructures have higher crystalline quality, surface-to-volume ratio, and elastic limit[14,15] and thus are more favorable to realize topological superconductivity and to investigate the Majorana Fermions.[16,17] However, to our best knowledge, the influence of size, strain and facet on the physical properties of strained Bi₂Se₃ nanoribbons has not been studied yet.

Micro-Raman spectroscopy is well established as a powerful and sensitive technique to characterize graphene-like layer materials.[18−24] Substrate,[25−27] thickness[28,29] and doping level[30,31] dependent *in situ* and

ex situ Raman spectra of Bi_2Se_3 ultrathin film and nanoplate have been reported. In this work, we report the strain, thickness and surface facet dependent phonon properties in individual Bi_2Se_3 nanoribbons. Utilizing the ultrafine glass tip of a micromanipulator, we strained tens of Bi_2Se_3 nanoribbons with thicknesses ranging from 70 to 500 nm. For a typical strain-free Bi_2Se_3 nanoribbon, all the four optical modes, the in-plane E_g^1 and E_g^2 modes and the out-of-plane A_{1g}^1 and A_{1g}^2 modes, are resolved in both Stokes and anti-Stokes Raman spectra. As expected, these modes soften with decreasing thickness, which is consistent with theoretical predictions.[25,26,28,32] In addition, a strong anisotropic behavior is observed for bent Bi_2Se_3 nanoribbon, due to the two structurally different facets, the $\{0001\}$ and the $\{01\bar{1}5\}$ surface, of Bi_2Se_3 nanoribbons grown along the $\langle 11\bar{2}0 \rangle$ direction.[33−36] Only when the nanoribbon is bent along the $\langle 11\bar{2}0 \rangle$ direction with the curved $\{0001\}$ surface perpendicular to the substrate plane and with the exposed $\{01\bar{1}5\}$ top surface do the frequencies of in-plane E_g^2 and out-of-plane A_{1g}^1 modes exhibit a linear blue-shift with increasing strain, which is also strongly thickness dependent. The phonon deformation potential (PDP) of the E_g^2 mode is up to 0.94 cm^{-1}/% for 100 nm-thick Bi_2Se_3 nanoribbon, while it is only approximately 0.52 cm^{-1}/% for Bi_2Se_3 bulk material.[37] Since the phonon modes stiffen linearly as the lattice is compressed,[37,38] the properties of the Bi_2Se_3 nanoribbons are more sensitive to strain than that of bulk materials. Our work indicates that thin Bi_2Se_3 nanoribbons are a promising candidate to study the strain modulated unique properties of the topological surface states.

RESULTS AND DISCUSSION

Raman Spectrum of Unstrained Bi_2Se_3 Nanoribbon. Bi_2Se_3 nanoribbons were synthesized by the Chemical Vapor Deposition (CVD) method,[39] and their thickness ranges from 70 to 500 nm while the length from tens to hundreds of micrometers (Figures S1 and S2). The single crystalline nature of Bi_2Se_3 nanoribbons was confirmed by transmission electron microscopy (TEM) (Figure S1b), high-resolution TEM (HRTEM) (Figure S1c) and selected area electron diffraction (SAED) patterns (Figure S1d). The growth direction of the Bi_2Se_3 nanoribbons is always along $\langle 11\bar{2}0 \rangle$. Figure 1a−c shows the scanning TEM (STEM) results of the cross-sectional sample of a nanoribbon, revealing the exposed facets of the as-grown nanoribbons. A TEM image of a representative cross-sectional sample is shown in Figure 1b at low magnification, and its side facet indicated by the blue box is enlarged in Figure 1a by a high resolution high-angle annular dark field (HAADF) STEM image. The Fast Fourier Transformation (FFT) pattern of Figure 1a is shown in Figure 1c, which reveals the two structurally inequivalent types of facets to be the $\{0001\}$ and the $\{01\bar{1}5\}$ surfaces.[35,36] Consequently, there are two possibilities to position the Bi_2Se_3 nanoribbons on the substrate: with the $\{0001\}$ surface parallel to the substrate plane (Figure 1d), or with the $\{01\bar{1}5\}$ surface parallel to the substrate (Figure 1e). Correspondingly, the nanoribbons can be bent in two different geometries. Later, we will discuss the Raman spectra of these two kinds of bent Bi_2Se_3 nanoribbons with different thicknesses. Surprisingly they exhibit a totally different strain response.

Bi_2Se_3 has a layered rhombohedral structure, which belongs to the space group D_{3d}^5 ($R\bar{3}m$) as shown in Figure 2a. Each unit cell includes five atomic layers in the sequence of SeII−Bi−SeI−Bi-SeII, which is often referred as quintuple layer (QL) with a dimension of $\sim$1 nm along c axis. Stacks of QLs are linked by weak van der Waals forces with a slightly covalent nature, while intra QL possess strong covalent bonds. Considering the symmetry of the space group D_{3d}^5, the primitive unit cell contains five atoms corresponding to the chemical formula of Bi_2Se_3. Accordingly, there are 15 lattice dynamical modes at the center of its Brillouin zone (q = 0), three of which are acoustic and 12 are optical modes. These 12 optical modes can be classified by the irreducible representations $\chi = 2E_g + 2A_{1g} + 2E_u + 2A_{1u}$.[32] According to the selection rules, $2A_{1u}$ and $2E_u$ are infrared-active, while $2A_{1g}$ and $2E_g$ are Raman-active modes.[31] The Raman tensors of the latter one are[31]

$$A_{1g} : \begin{pmatrix} a & 0 & 0 \\ 0 & a & 0 \\ 0 & 0 & b \end{pmatrix}$$

$$E_g : \begin{pmatrix} c & 0 & 0 \\ 0 & -c & d \\ 0 & d & 0 \end{pmatrix}, \begin{pmatrix} 0 & -c & -d \\ -c & 0 & 0 \\ -d & 0 & 0 \end{pmatrix} \quad (1)$$

The intensity of Raman scattering $I \sim |e_s \cdot R \cdot e_i|^2$ may be different for the $\{01\bar{1}5\}$ or the $\{0001\}$ surface perpendicular to the direction of incident light, where e_s and e_i represent the unit polarization vectors of scattered and incident light, respectively, and are related to the orientation of the sample.

The corresponding atomic displacements of the Raman-active modes are depicted in Figure 2b, where the E_g modes are 2-fold in-plane vibrational modes and the A_{1g} modes vibrating along the [0001] direction are out-of-plane modes. These two types of Raman-active modes can be distinguished by the nonzero off-diagonal components in the E_g Raman tensor. In Figure 2c, a typical unpolarized Raman spectrum of an unstrained Bi_2Se_3 nanoribbon is plotted consisting of both Stokes and anti-Stokes contributions. All four bulk vibrational modes E_g^1, A_{1g}^1, E_g^2 and A_{1g}^2 are observed, with the corresponding peak positions at 37.3, 70.4, 131.9, and 171.2 cm^{-1}. To determine the Raman peak position and the line width, all the Raman spectra are fitted by Lorentzian line shape.
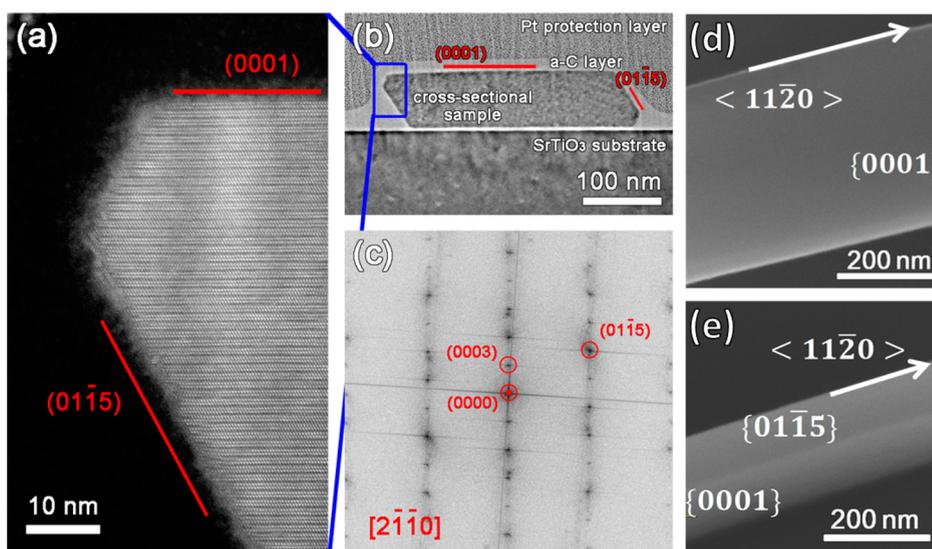
ARTICLE

Figure 1. Characterization of as grown Bi$_2$Se$_3$ nanoribbons. (a) High resolution HAADF-STEM image, (b) TEM image, and (c) the corresponding FFT pattern of (a) from a cross-sectional sample of Bi$_2$Se$_3$ nanoribbon. High magnification SEM image of Bi$_2$Se$_3$ nanoribbon (d) with the {0001} surface and (e) with the {01$\bar{1}$5} surface lying on the substrate.
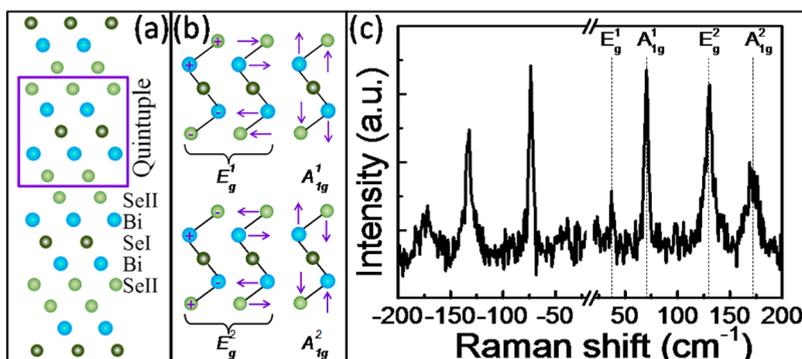

Figure 2. Crystal structure and Raman modes of Bi$_2$Se$_3$. (a) Layered structure of Bi$_2$Se$_3$. Five atomic layers in sequence of SeII–Bi–SeI–Bi–SeII as a repeating unit along c axis are indicated. (b) Schematic illustration of atomic displacements of bulk Bi$_2$Se$_3$ in Raman-active modes, where "+" and "-" correspond to the inward and outward vibrations perpendicular to the paper plane, respectively. (c) Typical Raman spectrum of a strain-free Bi$_2$Se$_3$ nanoribbon consisting of both Stokes and anti-Stokes contributions, where all four bulk vibrational modes are observed and marked.

Strain Dependent Raman Spectra of Bi$_2$Se$_3$ Nanoribbons with the {0001} Surface Parallel to the Substrate Plane. To investigate the influence of strain on the physical properties of topological insulator Bi$_2$Se$_3$ nanoribbons, a series of samples with various thickness and width are bent and measured. Figure 3a shows the scanning electron microscopy (SEM) image and scheme of a typical bent Bi$_2$Se$_3$ nanoribbon. To distinguish whether a given nanoribbon was lying either with its {0001} facets facing up and down on the substrate or the facets on the other long edge of the nanoribbon ({01$\bar{1}$5}) facing up and down, the sample was characterized by atomic force microscopy (AFM) to get the thickness and width. The width of this nanoribbon is 300 nm and the thickness is 180 nm. According to the STEM results, tens more cross-sectional Bi$_2$Se$_3$ nanoribbon samples with different sizes had been prepared, and we found, without an exception, the width of the samples is always larger than the thickness, which

implies that the {0001} facets are bigger than the {01$\bar{1}$5} facets. This can be easily understood by the growth mechanism. Because Bi$_2$Se$_3$ is a layered material, the in-plane growth is much easier than the growth along [0001] direction. For this sample shown in Figure 3a, the Bi$_2$Se$_3$ nanoribbon should be with the {0001} surface parallel to the substrate plane. Raman spectra collected from three different positions along the Bi$_2$Se$_3$ nanoribbon, marked by red, green, and blue color in Figure 3a, are shown in Figure 3b plotted with respective color. The frequencies of all four vibrational peaks E$_g^1$, A$_{1g}^1$, E$_g^2$ and A$_{1g}^2$ are denoted by the dashed lines.

Quantitatively, the maximum tensile and compressive strain ε_{ab}^{max} at the outer and inner side of the bent Bi$_2$Se$_3$ nanoribbon can be calculated by[40]

$$\varepsilon_{ab}^{max} = \frac{a - a_0}{a_0} = \pm \frac{d}{2R_{ab}} \quad (2)$$

YAN *ET AL.* VOL. 9 ■ NO. 10 ■ 10244–10251 ■ 2015 ACSNANO **10246**
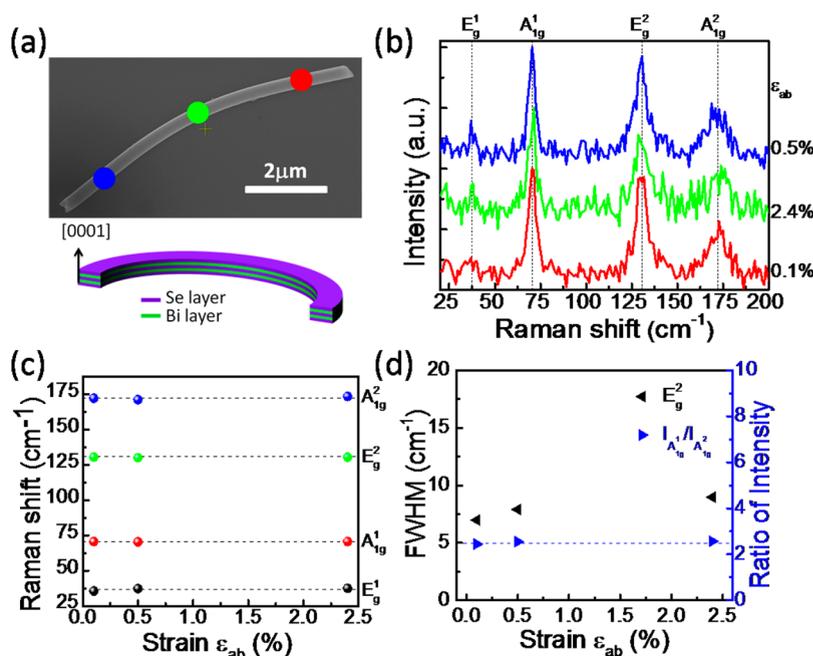www.acsnano.org

Figure 3. Raman spectra of a strained Bi_2Se_3 nanoribbon with the $\{0001\}$ surface parallel to the substrate plane. (a) SEM image and schematic illustration of a bent Bi_2Se_3 nanoribbon with a width of 300 nm and a thickness of 180 nm. The nanoribbon is bent along the $\langle 11\bar{2}0\rangle$ direction with the bending plane perpendicular to the $\{0001\}$ surface. (b) Raman spectra collected at different positions along the Bi_2Se_3 nanoribbon. The color of each curve corresponds to three different points on the Bi_2Se_3 nanoribbon. Frequencies of four vibrational modes are indicated by dashed lines. (c) Relationship of Raman shift of these four vibrational modes against strain. (d) The FWHM of E_g^2 mode and ratio of intensities $I_{A_{1g}^1}/I_{A_{1g}^2}$ as a function of strain.

where a and a_0 are the lattice constants of the sample in the strained and unstrained case, d is the width of the Bi_2Se_3 nanoribbon here, and R_{ab} is the radius of curvature with $R = \{[1 + (f')^2]^{3/2}/|yf''|\}$, where $y = f(x)$ is the curve function of bent Bi_2Se_3 nanoribbon. When the bending strain increases from 0 to 2.4%, the frequencies of all four vibrational modes E_g^1, A_{1g}^1, E_g^2 and A_{1g}^2 remain constant (Figure 3c). The full width at half-maximum (FWHM) of the in-plane E_g^2 peak exhibits a negligible increase from 6 to 8 cm^{-1} with increasing strain, while the ratio of Raman intensities $I_{A_{1g}^1}/I_{A_{1g}^2}$ does not change (Figure 3d). Considering the much larger spot size ($\sim$1 μm) of incident laser compared to the width of the nanoribbon, the contributions from the tensile outer side and the compressive inner side of the narrow nanoribbon will add up and cancel the frequency shift, as well as induce the broadening of the FWHM of the E_g^2 mode. As there is no strain along the [0001] direction in this case, the Raman intensity of the out-of-plane modes does not change with the bending strain ε_{ab}. Similar results of three more samples are shown in Figures S3–S5 in the Supporting Information.

Strain Dependent Raman Spectra of Bi_2Se_3 Nanoribbons with the Exposed $\{01\bar{1}5\}$ Top Surface on the Substrate. A typical SEM image and scheme of a bent 100 nm-thick Bi_2Se_3 nanoribbon are produced in Figure 4a, where the $\{0001\}$ surface is perpendicular to the substrate plane and the exposed top surface is the $\{01\bar{1}5\}$ surface. The nanoribbon is bent along the $\langle 11\bar{2}0\rangle$ direction with

the curved $\{0001\}$ surface. The Raman spectra are fitted by Lorentzian line shape and plotted in Figure 4b. Five curves with different colors correspond to the five positions on the Bi_2Se_3 nanoribbon marked by the same colors in Figure 4a. With increasing strain, the Raman frequencies of the A_{1g}^1 and E_g^2 features rise linearly, similar to the typical pressure-induced phonon stiffening.[37] The shear stress along c direction enhances the bond interaction by decreasing the bond length of Bi–SeI and SeII–SeII, resulting in the blue shift of the vibrational frequencies of the A_{1g}^1 and E_g modes. The corresponding PDP of these two modes are about 0.66 and 0.94 cm^{-1}/%, respectively (Figure 4c).

For a comparison, the reported PDP of the E_g^2 mode in bulk Bi_2Se_3 material under pressure (3.13 cm^{-1}/GPa)[37] can be converted to a strain value (%) by[40]

$$\frac{\partial \Delta \omega}{\partial \varepsilon} = (1 - 2\upsilon)E_{ab}\frac{\partial \Delta \omega}{\partial \sigma_{ab}} \tag{3}$$

The Poisson's ratio υ used here is 0.27, and the value of Young's modulus of Bi_2Se_3 bulk material along the $\langle 11\bar{2}0\rangle$ direction E_{ab} is 35.9 GPa;[41] thus, the PDP of bulk material is 0.52 cm^{-1}/%. It is worth noting that the frequency shift of the E_g^2 mode induced by the same strain in the Bi_2Se_3 nanoribbon is nearly twice of what is observed in bulk. In contrast to the blue-shift of the A_{1g}^1 and E_g^2 modes, the Raman frequencies of the A_{1g}^2 peak exhibit a red-shift with the PDP value about -1.78 cm^{-1}/%. The red-shift of the out-of-plane
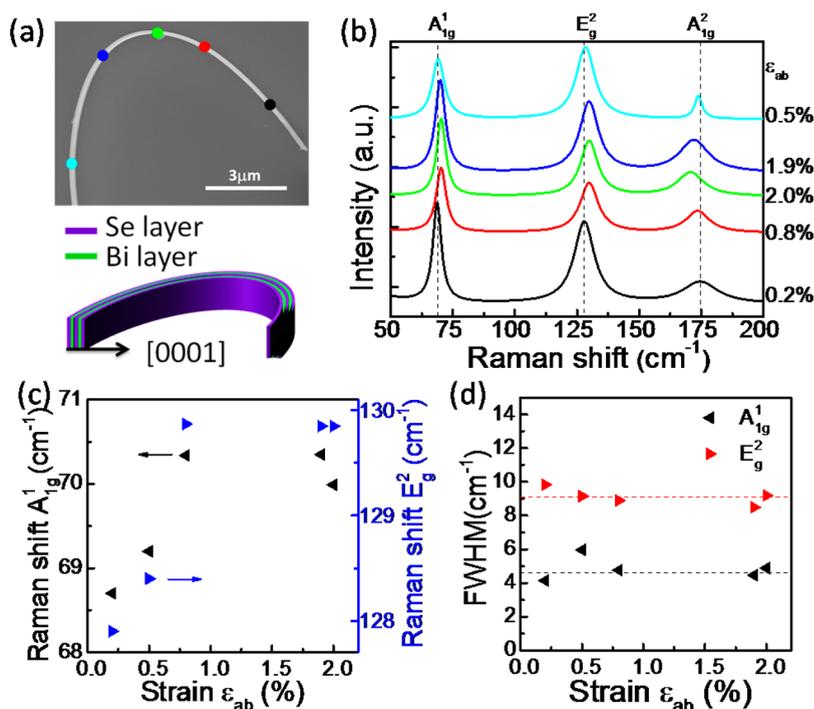
Figure 4. Raman spectra of a strained Bi_2Se_3 nanoribbon with the {0001} surface perpendicular to the substrate plane and the exposed {01$\bar{1}$5} top surface. (a) SEM image and schematic illustration of a bent Bi_2Se_3 nanoribbon with a thickness of 100 nm. The nanoribbon is bent along the ⟨11$\bar{2}$0⟩ direction with the curved {0001} surface. (b) Lorentzian fitted Raman spectra collected at different positions along the Bi_2Se_3 nanoribbon. The color of each curve corresponds to the five different points on this Bi_2Se_3 nanoribbon. (c) Relationship of Raman shift of the A_{1g}^1 and E_g^2 modes against strain. (d) The FWHM of the A_{1g}^1 and E_g^2 modes as a function of strain.

A_{1g}^2 mode may be caused by the strain modulation of the opposite vibrations of the Bi and Sell atoms.[28] The FWHM of both A_{1g}^1 and E_g^2 modes remains almost unchanged, implying that the phonon−phonon scattering stays the same (Figure 4d). Usually, the vibrational peaks broaden when contributions from tensile strain at outer surface and compressive strain at inner surface add up. On the other hand, the FWHM decreases when the strain-induced carrier concentration rises.[19] It has been reported that the carrier concentration of Bi_2Se_3 bulk materials is enhanced more than 10 times when the pressure increases from 0 to 10 GPa,[7] even without a structural phase transition. We conclude that the FWHM of both A_{1g}^1 and E_g^2 modes is unaltered as these two opposite effects cancel each other.

A series of bent Bi_2Se_3 nanoribbons with different thicknesses have been measured (Figures S6 and S7). As shown in Figure 5a, the Raman shift of the E_g^2 modes in 100, 120, 190, 220, and 260 nm-thick Bi_2Se_3 nanoribbons all exhibit a blue-shift with increasing strain. Some deviations from the linear relationship may be caused by the nonuniform interaction between Bi_2Se_3 nanoribbons and the substrate. The most interesting discovery is that the PDP of the E_g^2 feature increases with reducing the sample thickness (Figure 5b), which may arise from the surface effect.[14] Therefore, the strain modification on the phonon properties depends on the thickness of the Bi_2Se_3 nanoribbons strongly.

As reported, the relationship between the FWHM and thickness had been explained using exponential format.[32] Similarly, here we also use the exponential fit to thickness dependence of the PDP of E_g^2 mode in Figure 5b.

Thickness Dependent Raman Spectra of Strain-Free Bi_2Se_3 Nanoribbons. To explore the size effect in topological insulators, Raman spectra of three-dimensional (3D) bulk materials and 2D thin films have been collected,[3,25,28,29,32] where infrared features were observed due to the symmetry breaking in 2D thin film samples.[29,42] Here, quasi 1D Bi_2Se_3 nanoribbons with various thicknesses are measured to further investigate the size effect.

In Figure 6a, the Raman peak positions of individual Bi_2Se_3 nanoribbons are plotted as a function of the sample thickness. When the thicknesses d of unstrained Bi_2Se_3 nanoribbons decreases from 500 to 70 nm, the frequencies of both A_{1g}^1 and E_g^2 modes exhibit a red-shift about 4 cm^{-1}, which is consistent with previous results of thin film materials.[25,28,32,43] Considering the phonon confinement effects, the red-shift would relate to the surface-to-volume ratio, or $1/d$.[44,45] Then, the relationship of the frequency and d can be fitted by[32,44]

$$\omega(d) = \omega(0) - A/d \qquad (4)$$

where $\omega(0)$ is the phonon frequency in the bulk (Figure 6a). Meanwhile, the surface relaxation and
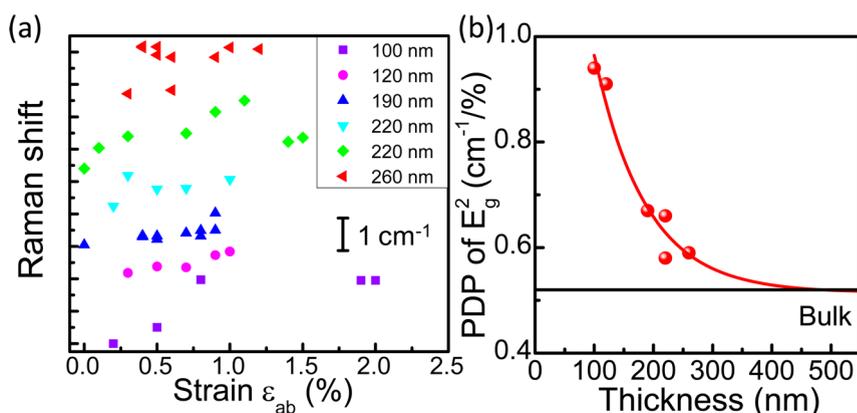
Figure 5. Thickness dependent Raman shift of strained Bi_2Se_3 nanoribbons with the $\{0001\}$ surface perpendicular to the substrate plane and the exposed $\{01\bar{1}5\}$ top surface. (a) Relationship of strain and Raman shift of E_g^2 modes of 100, 120, 190, 220, 260 nm thick Bi_2Se_3 nanoribbons, and the data have been shifted up by a constant value to make it clear. (b) The phonon deformation potential (PDP) of E_g^2 mode *versus* the thickness of Bi_2Se_3 nanoribbons. The red line is the fit by an exponential function. The bold black line indicates the PDP value of Bi_2Se_3 bulk material from ref 37.
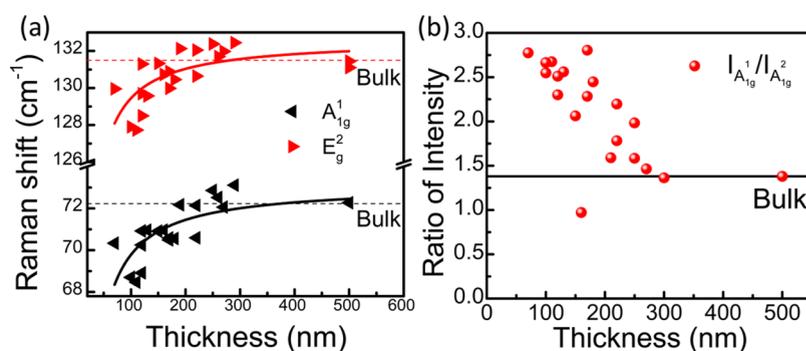

Figure 6. Thickness dependent Raman spectra of strain-free Bi_2Se_3 nanoribbons. (a) Raman shift of A_{1g}^1 and E_g^2 modes *versus* thickness. The black (red) solid line is fitting curve of A_{1g}^1 (E_g^2) mode. (b) Ratio of intensities $I_{A_{1g}^1}/I_{A_{1g}^2}$ *versus* thickness. The bold lines indicate the corresponding value of Bi_2Se_3 bulk material from ref 31.

structural defects should also be considered to explain the red-shift.

The ratio of the Raman intensities $I_{A_{1g}^1}/I_{A_{1g}^2}$ increases as the thickness is reduced, in contrast to the results reported for thin films.[32] Considering the surface tension in the nanostructure with large surface-to-volume ratio, the strength of the out-of-plane vibration A_{1g}^1 mode should be enhanced by decreasing thickness, as shown in Figure 6b.

DISCUSSION

Our systematic investigations of the strain, thickness and surface facet dependent Raman spectra of Bi_2Se_3 nanoribbons yield the basis for some important points. For strain-free samples, all the optical phonon frequencies become red-shifted as the sample thickness is reduced, due to the increased phonon confinement effect and surface tension, which is insensitive to the way the nanoribbons are placed on the substrate, while for strained samples with the $\{0001\}$ or the $\{01\bar{1}5\}$ surface parallel to the substrate plane, strong anisotropies are observed, caused by the different bending loading method on the nanoribbon.

The strain induced anisotropy demonstrates that Raman spectra of Bi_2Se_3 nanoribbon are more sensitive to the stress along *c* direction. Furthermore, the PDP of the E_g^2 mode of Bi_2Se_3 nanoribbon was found to increase with decreasing the nanoribbon thickness. Therefore, a much lower critical pressure (stress) is expected to be sufficient to induce a superconducting phase transition in thin Bi_2Se_3 nanoribbons compared to the bulk counterpart. With the use of this great advantage of nanostructures, a superconducting dome was observed recently in WTe_2 nanoflakes with a pressure even smaller than 5 GPa.[46]

CONCLUSIONS

In conclusion, the influence of size and strain on the Raman spectra of topological insulator Bi_2Se_3 nanoribbons is investigated systematically. All four optical modes, the in-plane E_g^1 and E_g^2, and out-of-plane A_{1g}^1 and A_{1g}^2 modes, are resolved in both Stokes and anti-Stokes Raman spectra, and they all soften as the thickness of unstrained Bi_2Se_3 nanoribbons reduces, while for bent Bi_2Se_3 nanoribbons, a strong anisotropy is observed, due to the differences in the exposed top

facets on the substrate: the {0001} and the {01$\bar{1}$5} surfaces. Only when the {0001} surface is perpendicular to the substrate plane and the exposed top surface is the {01$\bar{1}$5} surface, that is, the nanoribbon is bent along the ⟨11$\bar{2}$0⟩ direction with the curved {0001} surface, the E_g^2 and A_{1g}^1(A_{1g}^2) modes of the Bi$_2$Se$_3$ nanoribbon show a blue-shift (red-shift) with strain, and the phonon deformation potential of the E_g^2 mode rises nonlinearly with decreasing sample thickness. The results are helpful for further investigations on the quantum transport of strained Bi$_2$Se$_3$ nanostructures.

MATERIALS AND METHODS

Synthesis of Bi$_2$Se$_3$ Nanoribbons. Bi$_2$Se$_3$ nanoribbons were synthesized by CVD method. Bi$_2$Se$_3$ powder (Alfa Aesar) with high purity (>99.99%) was put in the center of a horizontal tube furnace (Lindberg/Blue M) as the source, while several undoped silicon pieces with 5 nm gold film deposited by electron beam evaporation were placed downstream approximately 9 cm away from the source as the collecting substrates. High purity Ar gas was used to pump and flush the tube, maintain the inside pressure and carry the source vapor from central hot zone (700 °C) to the cold edge (about 350 °C). After the growth, desirable Bi$_2$Se$_3$ nanoribbons were chose from the as-grown products, transferred onto the Si/SiO$_2$ substrate with marks, and then manipulated to be curved under an optical microscope with micromanipulator by using two needle-shaped glass tips.

Characterization of Bi$_2$Se$_3$ Nanoribbons. The as-synthesized Bi$_2$Se$_3$ nanoribbons were characterized by the field-emission SEM (FEI NanoSEM 430) with the accelerating voltage 10 kV. The Bi$_2$Se$_3$ nanoribbons were transferred onto a copper grid by gently rubbing it on an as-grown substrate and then characterized by 200 kV field-emissions TEM (Tecnai G2 F20). To prepare the cross-sectional TEM sample, 10 more Bi$_2$Se$_3$ nanoribbons were transferred onto SrTiO$_3$ substrate. The nanoribbons were randomly chosen using focused ion beam (FIB, FEI Helios NanoLab DualBeam system). Amorphous carbon/Pt protection layer was deposited to protect the Bi$_2$Se$_3$ nanoribbon surface by electron beam induced deposition method in the FIB system. Then, the Bi$_2$Se$_3$ nanoribbon was cut along the cross-section by the FIB and then transferred onto a TEM grid by a nanomanipulator in the FIB system. HAADF-STEM was performed using an FEI Titan Cube 60-300 microscope fitted with an aberration corrector for the probe forming lens operated at 200 kV.

Raman Spectral Measurement. Unpolarized Raman spectra of the Bi$_2$Se$_3$ nanoribbons were measured by a home-built confocal micro-Raman microscopy system (Princeton Instruments Acton SP 2500i) in the backscattering configuration at room temperature. The Raman spectra are excited by a λ = 532 nm solid state laser with high power stability. The focused spot size is about 1 μm, the spectra resolution ~1 cm^{-1} and the lowest available frequency is better than 20 cm^{-1} by a set of 532 nm BragGrate Notch Filter (532 BNF). The incident laser power after the 100× objective (N.A. = 0.90) is about 0.2 mW to avoid sample damage or laser-induced heating. Each spectrum is collected for 3 min, because the signal of the nanoribbon is relatively small.

Conflict of Interest: The authors declare no competing financial interest.

Supporting Information Available: The Supporting Information is available free of charge on the ACS Publications website at DOI: 10.1021/acsnano.5b04057.

SEM picture of as-synthesized Bi$_2$Se$_3$ nanoribbons. Typical TEM, HRTEM images and SAED patterns of a strain-free Bi$_2$Se$_3$ nanoribbon. Typical AFM image of a strained Bi$_2$Se$_3$ nanoribbon. Raman spectra of strained Bi$_2$Se$_3$ nanoribbons with different thicknesses in two cases (PDF)

REFERENCES AND NOTES

1. Fu, L.; Kane, C. L.; Mele, E. J. Topological Insulators in Three Dimensions. *Phys. Rev. Lett.* **2007**, *98*, 106803.
2. Kane, C. L.; Mele, E. J. Quantum Spin Hall Effect in Graphene. *Phys. Rev. Lett.* **2005**, *95*, 226801.
3. Moore, J. E.; Balents, L. Topological Invariants of Time-Reversal-Invariant Band Structures. *Phys. Rev. B: Condens. Matter Mater. Phys.* **2007**, *75*, 121306(R).
4. Qi, X.-L.; Zhang, S.-C. Topological Insulators and Superconductors. *Rev. Mod. Phys.* **2011**, *83*, 1057.
5. König, M.; Wiedmann, S.; Brüne, C.; Roth, A.; Buhmann, H.; Molenkamp, L. W.; Qi, X.-L.; Zhang, S.-C. Quantum Spin Hall Insulator State in HgTe Quantum Wells. *Science* **2007**, *318*, 766–770.
6. Zhang, H.; Liu, C.-X.; Qi, X.-L.; Dai, X.; Fang, Z.; Zhang, S.-C. Topological Insulators in Bi$_2$Se$_3$, Bi$_2$Te$_3$ and Sb$_2$Te$_3$ with a Single Dirac Cone on the Surface. *Nat. Phys.* **2009**, *5*, 438–442.
7. Kirshenbaum, K.; Syers, P.; Hope, A.; Butch, N.; Jeffries, J.; Weir, S.; Hamlin, J.; Maple, M.; Vohra, Y.; Paglione, J. Pressure-Induced Unconventional Superconducting Phase in the Topological Insulator Bi$_2$Se$_3$. *Phys. Rev. Lett.* **2013**, *111*, 087001.
8. Zhao, J.; Liu, H.; Ehm, L.; Dong, D.; Chen, Z.; Gu, G. High-Pressure Phase Transitions, Amorphization, and Crystallization Behaviors in Bi$_2$Se$_3$. *J. Phys.: Condens. Matter* **2013**, *25*, 125602.
9. Zhang, J.; Zhang, S.; Weng, H.; Zhang, W.; Yang, L.; Liu, Q.; Feng, S.; Wang, X.; Yu, R.; Cao, L.; et al. Pressure-Induced Superconductivity in Topological Parent Compound Bi$_2$Te$_3$. *Proc. Natl. Acad. Sci. U. S. A.* **2011**, *108*, 24–28.
10. Zhang, C.; Sun, L.; Chen, Z.; Zhou, X.; Wu, Q.; Yi, W.; Guo, J.; Dong, X.; Zhao, Z. Phase Diagram of a Pressure-Induced Superconducting State and its Relation to the Hall Coefficient of Bi$_2$Te$_3$ Single Crystals. *Phys. Rev. B: Condens. Matter Mater. Phys.* **2011**, *83*, 140504.
11. Buga, S.; Kulbachinskii, V.; Kytin, V.; Kytin, G.; Kruglov, I.; Lvova, N.; Perov, N.; Serebryanaya, N.; Tarelkin, S.; Blank, V. Superconductivity in Bulk Polycrystalline Metastable Phases of Sb$_2$Te$_3$ and Bi$_2$Te$_3$ Quenched after High-Pressure—High-Temperature Treatment. *Chem. Phys. Lett.* **2015**, *631*, 97–102.
12. Levy, N.; Zhang, T.; Ha, J.; Sharifi, F.; Talin, A. A.; Kuk, Y.; Stroscio, J. A. Experimental Evidence for s-Wave Pairing Symmetry in Superconducting Cu$_x$Bi$_2$Se$_3$ Single Crystals using a Scanning Tunneling Microscope. *Phys. Rev. Lett.* **2013**, *110*, 117001.
13. Hsieh, T. H.; Fu, L. Majorana Fermions and Exotic Surface Andreev Bound States in Topological Superconductors: Application to Cu$_x$ Bi$_2$Se$_3$. *Phys. Rev. Lett.* **2012**, *108*, 107005.
14. Fu, X.-W.; Liao, Z.-M.; Liu, R.; Xu, J.; Yu, D. Size-Dependent Correlations between Strain and Phonon Frequency in Individual ZnO Nanowires. *ACS Nano* **2013**, *7*, 8891–8898.
15. van der Zande, A.; Hone, J. Optical Materials: Inspired by Strain. *Nat. Photonics* **2012**, *6*, 804–806.
16. Rokhinson, L. P.; Liu, X.; Furdyna, J. K. The Fractional ac Josephson Effect in a Semiconductor-Superconductor Nanowire as a Signature of Majorana Particles. *Nat. Phys.* **2012**, *8*, 795–799.
17. Mourik, V.; Zuo, K.; Frolov, S.; Plissard, S.; Bakkers, E.; Kouwenhoven, L. Signatures of Majorana Fermions in

Hybrid Superconductor-Semiconductor Nanowire Devices. *Science* **2012**, *336*, 1003–1007.

18. Pisana, S.; Lazzeri, M.; Casiraghi, C.; Novoselov, K. S.; Geim, A. K.; Ferrari, A. C.; Mauri, F. Breakdown of the Adiabatic Born−Oppenheimer Approximation in Graphene. *Nat. Mater.* **2007**, *6*, 198–201.

19. Das, A.; Pisana, S.; Chakraborty, B.; Piscanec, S.; Saha, S.; Waghmare, U.; Novoselov, K.; Krishnamurthy, H.; Geim, A.; Ferrari, A.; et al. Monitoring Dopants by Raman Scattering in an Electrochemically Top-Gated Graphene Transistor. *Nat. Nanotechnol.* **2008**, *3*, 210–215.

20. Coleman, J. N.; Lotya, M.; O'Neill, A.; Bergin, S. D.; King, P. J.; Khan, U.; Young, K.; Gaucher, A.; De, S.; Smith, R. J.; et al. Two-Dimensional Nanosheets Produced by Liquid Exfoliation of Layered Materials. *Science* **2011**, *331*, 568–571.

21. Malard, L.; Pimenta, M.; Dresselhaus, G.; Dresselhaus, M. Raman Spectroscopy in Graphene. *Phys. Rep.* **2009**, *473*, 51–87.

22. Tan, P.; Han, W.; Zhao, W.; Wu, Z.; Chang, K.; Wang, H.; Wang, Y.; Bonini, N.; Marzari, N.; Pugno, N.; et al. The Shear Mode of Multilayer Graphene. *Nat. Mater.* **2012**, *11*, 294–300.

23. Safdar, M.; Wang, Q.; Mirza, M.; Wang, Z.; Xu, K.; He, J. Topological Surface Transport Properties of Single-Crystalline SnTe Nanowire. *Nano Lett.* **2013**, *13*, 5344–5349.

24. Zhang, X.; Qiao, X.-F.; Shi, W.; Wu, J.-B.; Jiang, D.-S.; Tan, P.-H. Phonon and Raman Scattering of Two-Dimensional Transition Metal Dichalcogenides from Monolayer, Multilayer to Bulk Material. *Chem. Soc. Rev.* **2015**, *44*, 2757–2785.

25. Dang, W.; Peng, H.; Li, H.; Wang, P.; Liu, Z. Epitaxial Heterostructures of Ultrathin Topological Insulator Nanoplate and Graphene. *Nano Lett.* **2010**, *10*, 2870–2876.

26. Zhao, Y.; Luo, X.; Zhang, J.; Wu, J.; Bai, X.; Wang, M.; Jia, J.; Peng, H.; Liu, Z.; Quek, S. Y.; et al. Interlayer Vibrational Modes in Few-Quintuple-Layer Bi_2Te_3 and Bi_2Se_3 Two-Dimensional Crystals: Raman Spectroscopy and First-Principles Studies. *Phys. Rev. B: Condens. Matter Mater. Phys.* **2014**, *90*, 245428.

27. Shahil, K.; Hossain, M.; Goyal, V.; Balandin, A. Micro-Raman Spectroscopy of Mechanically Exfoliated Few-Quintuple Layers of Bi_2Te_3, Bi_2Se_3, and Sb_2Te_3 Materials. *J. Appl. Phys.* **2012**, *111*, 054305.

28. Wang, C.; Zhu, X.; Nilsson, L.; Wen, J.; Wang, G.; Shan, X.; Zhang, Q.; Zhang, S.; Jia, J.; Xue, Q. *In situ* Raman Spectroscopy of Topological Insulator Bi_2Te_3 Films with Varying Thickness. *Nano Res.* **2013**, *6*, 688–692.

29. He, R.; Wang, Z.; Qiu, R. L.; Delaney, C.; Beck, B.; Kidd, T.; Chancey, C.; Gao, X. P. Observation of Infrared-Active Modes in Raman Scattering from Topological Insulator Nanoplates. *Nanotechnology* **2012**, *23*, 455703.

30. Soni, A.; Yanyuan, Z.; Ligen, Y.; Aik, M. K. K.; Dresselhaus, M. S.; Xiong, Q. Enhanced Thermoelectric Properties of Solution Grown $Bi_2Te_{3-x}Se_x$ Nanoplatelet Composites. *Nano Lett.* **2012**, *12*, 1203–1209.

31. Richter, W.; Becker, C. A Raman and Far-Infrared Investigation of Phonons in the Rhombohedral V2−VI3 Compounds Bi_2Te_3, Bi_2Se_3, Sb_2Te_3 and $Bi_2(Te_{1-x}Se_x)_3$ (0< x< 1), $(Bi_{1-y}Sb_y)_2Te_3$ (0< y< 1). *Phys. Status Solidi B* **1977**, *84*, 619–628.

32. Zhang, J.; Peng, Z.; Soni, A.; Zhao, Y.; Xiong, Y.; Peng, B.; Wang, J.; Dresselhaus, M. S.; Xiong, Q. Raman Spectroscopy of Few-Quintuple Layer Topological Insulator Bi_2Se_3 Nanoplatelets. *Nano Lett.* **2011**, *11*, 2407–2414.

33. Chen, F.; Jauregui, L.; Tan, Y.; Manfra, M.; Chen, Y.; Gerhard, K.; Kubis, T. In-Surface Confinement of Topological Insulator Nanowire Surface States. **2015**, *arXiv:1505.04153*.

34. Yan, Y.; Liao, Z.-M.; Ke, X.; Van Tendeloo, G.; Wang, Q.; Sun, D.; Yao, W.; Zhou, S.; Zhang, L.; Wu, H.-C.; et al. Topological Surface State Enhanced Photothermoelectric Effect in Bi_2Se_3 Nanoribbons. *Nano Lett.* **2014**, *14*, 4389–4394.

35. Yan, Y.; Wang, L.-X.; Ke, X.; Van Tendeloo, G.; Wu, X.-S.; Yu, D.-P.; Liao, Z.-M. High-Mobility Bi_2Se_3 Nanoplates Manifesting Quantum Oscillations of Surface States in the Sidewalls. *Sci. Rep.* **2014**, *4*, 3817.

36. Medlin, D.; Ramasse, Q.; Spataru, C.; Yang, N. Structure of the (0001) Basal Twin Boundary in Bi_2Te_3. *J. Appl. Phys.* **2010**, *108*, 043517.

37. Vilaplana, R.; Santamaría-Pérez, D.; Gomis, O.; Manjón, F.; González, J.; Segura, A.; Munoz, A.; Rodríguez-Hernández, P.; Pérez-González, E.; Marín-Borrás, V.; et al. Structural and Vibrational Study of Bi_2Se_3 under High Pressure. *Phys. Rev. B: Condens. Matter Mater. Phys.* **2011**, *84*, 184110.

38. Kong, P.; Zhang, J.; Zhang, S.; Zhu, J.; Liu, Q.; Yu, R.; Fang, Z.; Jin, C.; Yang, W.; Yu, X.; et al. Superconductivity of the Topological Insulator Bi_2Se_3 at High Pressure. *J. Phys.: Condens. Matter* **2013**, *25*, 362204.

39. Yan, Y.; Liao, Z.-M.; Zhou, Y.-B.; Wu, H.-C.; Bie, Y.-Q.; Chen, J.-J.; Meng, J.; Wu, X.-S.; Yu, D.-P. Synthesis and Quantum Transport Properties of Bi_2Se_3 Topological Insulator Nanostructures. *Sci. Rep.* **2013**, *3*, 1264.

40. Dietrich, C.; Lange, M.; Klüpfel, F.; Von Wenckstern, H.; Schmidt-Grund, R.; Grundmann, M. Strain Distribution in Bent ZnO Microwires. *Appl. Phys. Lett.* **2011**, *98*, 031105.

41. Koc, H.; Ozisik, H.; Deligöz, E.; Mamedov, A. M.; Ozbay, E. Mechanical, Electronic, and Optical Properties of Bi_2S_3 and Bi_2Se_3 Compounds: First Principle Investigations. *J. Mol. Model.* **2014**, *20*, 1–12.

42. Shahil, K.; Hossain, M.; Teweldebrhan, D.; Balandin, A. Crystal Symmetry Breaking in Few-Quintuple Bi_2Te_3 Films: Applications in Nanometrology of Topological Insulators. *Appl. Phys. Lett.* **2010**, *96*, 153103.

43. Hepting, M.; Kukuruznyak, D.; Benckiser, E.; Le Tacon, M.; Keimer, B. Raman Light Scattering on Ultra-Thin Films of $LaNiO_3$ under Compressive Strain. *Phys. B* **2015**, *460*, 196–198.

44. Yang, C.; Li, S. Size-Dependent Raman Red Shifts of Semiconductor Nanocrystals. *J. Phys. Chem. B* **2008**, *112*, 14193–14197.

45. Adu, K.; Gutierrez, H.; Kim, U.; Sumanasekera, G.; Eklund, P. Confined Phonons in Si Nanowires. *Nano Lett.* **2005**, *5*, 409–414.

46. Pan, X.-C.; Chen, X.; Liu, H.; Feng, Y.; Song, F.; Wan, X.; Zhou, Y.; Chi, Z.; Yang, Z.; Wang, B.; et al. Pressure-Induced Superconductivity in WTe_2. **2015**, *arXiv:1501.07394*.